INORGANIC
CHEMISTRY

FRONTIERS

View Article Online
View Journal | View Issue

A proof-of-concept application of water-soluble ytterbium(III) molecular probes in *in vivo* NIR-II whole body bioimaging†

Yingying Ning, [iD] ‡[a] Si Chen,‡[b,c] Hao Chen,[b] Jing-Xiang Wang,[a] Shuqing He,[b] Yi-Wei Liu,[a] Zhen Cheng [iD] *[b] and Jun-Long Zhang [iD] *[a]

Near-infrared (NIR) emissive lanthanide (Ln) complexes are promising candidates for fluorescence imaging in the NIR-II region (1000–1700 nm) to combine the advantages of small organic molecules and inorganic metal ions. However, their metabolism *in vivo* and application in *in vivo* imaging are still unknown. In this work, we used water-soluble Yb^{3+} molecular probes with a quantum yield of *ca.* 10% in water, which showed a deep penetration (>3 mm) upon excitation at the Q band. One of the Yb^{3+} complexes, **Yb-2**, was successfully applied in high resolution non-invasive whole body, vasculature and lymph node imaging of small animals. The complex cleared from the body through hepatobiliary and renal systems, similar to most organic fluorophores. Importantly, we demonstrated the application of **Yb-2** in fluorescence-guided sentinel lymph node surgery, showing the prospective application of lanthanide complexes as molecular probes in NIR-II whole body bioimaging and surgical operation.

Introduction

Fluorescence imaging allows non-invasive, sensitive and high resolution monitoring of many early events in carcinogenesis and a wide range of biological processes *in vivo*. Compared to traditional fluorescence imaging in the visible and NIR-I regions (400–900 nm), imaging at the second near-infrared window (NIR-II, 1000–1700 nm) dramatically reduced tissue absorption, autofluorescence and photon scattering.[1,2] Consequently, fluorescence imaging in the NIR-II window can achieve deeper tissue penetration and higher spatial and temporal resolution than those in the NIR-I window.[3,4] In recent years, organic molecules,[5–8] carbon nanotubes,[9] quantum dots[10,11] and upconversion nanoparticles[12–14] have been used for NIR-II *in vivo* imaging, particularly in the real-time vasculature visualization and removal of sentinel lymph

nodes and tumors. However, organic dyes generally suffer from problems such as easy photobleaching and small Stokes shift; on the other hand, inorganic nanomaterials are limited by their unknown toxicity concerns and slow excretion pharmacokinetics arising from their sizes.[15,16]

To circumvent the photostability of organic molecules and large size in inorganic nanoparticles, NIR-II emissive lanthanide (Ln) complexes are promising candidates due to their small sizes and metal-centered emission.[17,18] These features endow them with *f–f* characteristic emission, large Stokes shift and high photo- and/or chemostability.[19,20] However, Ln NIR luminescence is easily quenched by high energy X–H bond (X = C, N and O) vibration arising from ligands and solvents.[21–23] Only a very limited number of NIR Ln molecular probes have previously been applied in cell imaging due to their low quantum yields (below 3% in water),[24–28] although many visible Ln molecular probes have been investigated for bioimaging before.[29–33] Even to date, *in vivo* imaging using NIR Ln molecular probes with antenna ligands has not been achieved for the inefficient antenna effect, although the design of NIR probes for bioanalysis started two decades ago.[34–36] To overcome this challenge, we recently reported perfluorinated Yb^{3+} porphyrinates emitted with unprecedented high quantum yields (*ca.* 25%) in the NIR region (900–1100 nm).[37,38] Moreover, after subsequent modifications to improve their biocompatibility, the quantum yields of Yb^{3+} complexes reached 5–13% in water, thus they can be applied in live cell imaging.[39] Their long decay lifetimes also allowed them to be successfully applied in

[a]Beijing National Laboratory for Molecular Sciences, State Key Laboratory of Rare Earth Materials Chemistry and Applications, College of Chemistry and Molecular Engineering, Peking University, Beijing 100871, P. R. China.
E-mail: zhangjunlong@pku.edu.cn
[b]Molecular Imaging Program at Stanford (MIPS), Bio-X Program, and Department of Radiology, Canary Center at Stanford for Cancer Early Detection, Stanford University, California 94305-5344, USA. E-mail: zcheng@stanford.edu
[c]Department of Neurology, Xiangya Hospital, Central South University, Xiangya Road 88, Changsha, Hunan 410008, P. R. China.
†Electronic supplementary information (ESI) available. See DOI: 10.1039/c9qi00157c
‡These authors contributed equally.

time-resolved fluorescence lifetime imaging recently.[40] However, the behaviour of the Yb^{3+} complexes *in vivo* is still unknown. Therefore, the next endeavour is to answer the crucial questions such as whether Yb^{3+} porphyrinates can be employed in NIR-II *in vivo* whole body bioimaging, which is critical to demonstrate their potential applications as theragnostic agents eventually for clinical translation.

Herein we report a proof-of-concept work using water-soluble Yb^{3+} molecular probes for *in vivo* whole body bioimaging. According to a previous report, we synthesized cationic phosphoniums[39] and anionic carboxylate Yb^{3+} porphyrinates[40] with quantum yields of *ca.* 10% in water. Combining with the large extinction coefficient of the porphyrin ligand, **Yb-2**, with carboxylate modification, presents high *in vivo* luminescence and achieves high resolution vasculature imaging in small animals. By using a 1000 nm longpass filter, Yb^{3+} porphyrinates have been demonstrated to help the image-guided operation in the NIR-II region using mice models. Therefore, this work provides a foundation and insight into the design of NIR *in vivo* imaging molecular probes using emissive Ln coordination compounds and enriches the repertoire of the chemical biology of Ln compounds.

Results and discussion

According to a previous report, we prepared **Yb-2** and **Yb-3** as water-soluble Yb^{3+} porphyrinates with carboxylate and cationic phosphoniums, respectively (Fig. 1a).[39,40] Ester group containing **Yb-1**, which is not water-soluble, was used as control. The absorption spectra of Yb^{3+} complexes in DMSO and H_2O are similar and display an intense Soret band centered at *ca.* 410 nm and Q bands between 520–650 nm (Fig. 1b and S1†). It is noteworthy that the extinction coefficient (ε) of the Q band in the range of *ca.* 525–620 nm is larger than 10^4 M^{-1} cm^{-1} for **Yb-2**. Upon excitation at the Soret or Q band, **Yb-1–3** exhibited intense characteristic $^2F_{5/2} \rightarrow {}^2F_{7/2}$ transition bands of Yb^{3+} at 900–1100 nm. The fluorescence quantum yields of **Yb-1–3** in DMSO were *ca.* 20–22%, with long decay lifetimes of *ca.* 205–220 μs (Fig. S2†). Importantly, compared to **Yb-3** (Φ_{Yb} = 5.1%, τ_{obs} = 56 μs in H_2O), **Yb-2** presented a higher quantum

yield (10%, Fig. 1c) and lifetime (140 μs) in H_2O (Fig. S3†), with the brightness ($\varepsilon*\Phi$) of *ca.* 10^3 M^{-1} cm^{-1}. Although complex **Yb-2** is pH-sensitive, it still maintains a high luminescence and lifetime (100 μs) in serum. For **Yb-3**, the NIR emission is not pH-sensitive (Fig. S4†). More importantly, from the NIR-II images in water (Fig. 1d), we can observe a strong NIR-II luminescence from **Yb-2** and **Yb-3** even under the excitation at 520 nm (Q band).

Yb-2 and **Yb-3** showed high stability in water, phosphate buffer saline (PBS), and fetal bovine serum (FBS) under basic and acidic conditions (Fig. S5 and 6†). Importantly, we found that the complexes showed significantly higher photostability than a commercial NIR fluorophore (Cy5.5), when taking **Yb-2** as an example (Fig. S7†). Although the complexes showed lower NIR brightness than that of Cy 5.5 (*ca.* 10^4 M^{-1} cm^{-1}), they are still promising for *in vivo* imaging due to their strong resistance to photobleaching. The standard CCK-8 assay also indicated the low dark cytotoxicity and photocytotoxicity of **Yb-2** and **Yb-3** towards HeLa cells (Fig. S8†).

As **Yb-2** shows a higher NIR quantum yield than **Yb-3**, before its application in *in vivo* bioimaging, we investigated the NIR-II penetration depth by covering pork of different thicknesses (0, 4 and 8 mm) in the water solution of **Yb-2** as an example. As shown in Fig. 2, upon excitation at the Q band (532 nm), the NIR-II luminescence signals decreased with the
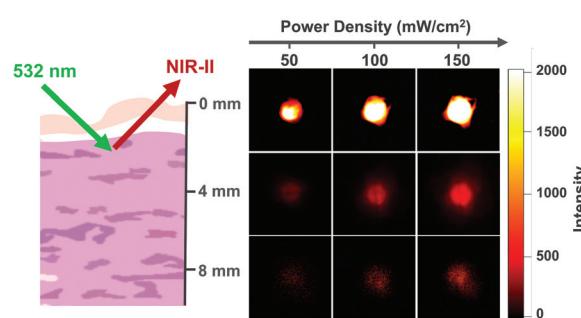
Fig. 2 Luminescence intensity of **Yb-2** (2 mg mL^{-1}) in the NIR-II region (100 ms exposure, 1000 nm longpass filter) under the corresponding penetration depth (0, 4 and 8 mm) and excitation laser power (532 nm, 50, 100 and 150 mW cm^{-2}).
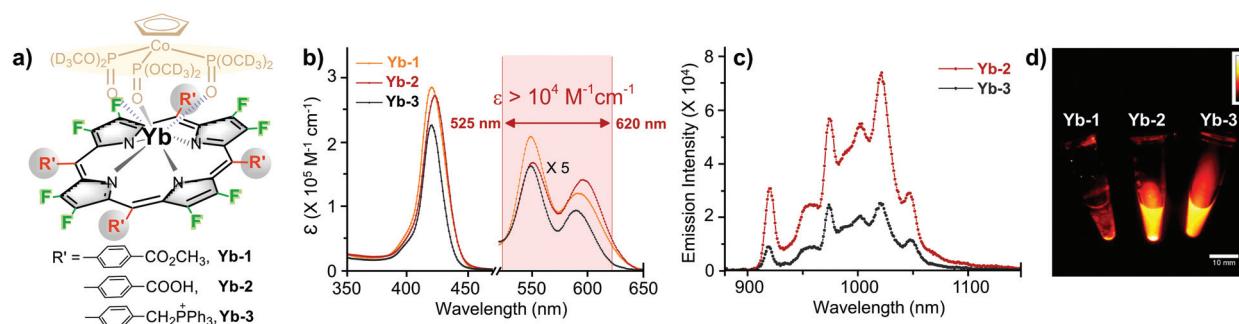
Fig. 1 (a) Structures of the Yb^{3+} complexes studied in this work. (b) Normalized absorption spectra of **Yb-1–3** in DMSO; (c) Emission spectra of **Yb-2** and **Yb-3** in water (λ_{ex} = 410 nm, $A_{410\ nm}$ = 0.1); (d) NIR-II fluorescence image of an aqueous solution of **Yb-1** to **Yb-3** under the excitation of 520 nm (1000 nm longpass filter).

increasing pork thickness and decreasing excitation laser power. However, the signals were still collected even with the block of 8 mm pork and using 50 mW cm^{-2} excitation laser power, which should benefit from the high luminescence of **Yb-2**. These results strongly demonstrate the deep penetration ability of the **Yb-2** luminescence in the NIR-II region.

Based on *in vitro* results, we then performed whole-body NIR-II imaging of C57BL/6 mice with the injection of **Yb-2** using a 1000 nm longpass filter under the excitation of a 520 nm laser. Immediately after tail vein injection, superior vasculature and whole body imaging were visualized from the surrounding background tissue due to the reduced scattering, tissue absorption and autofluorescence in the NIR-II window, as shown in Fig. 3. After 12 h post-injection, an *ex vivo* biodistribution study was performed to evaluate the biodistribution of the complex in the major organs. The results showed that **Yb-2** mainly accumulated in kidneys and intestines. A small fraction of probe signal was also detected in the liver and no signals were observed in muscles, matching with the *in vivo* fluorescence results. These indicate that the clearance routes of the Yb^{3+} complexes are through both hepatobiliary and renal systems, similar to most organic fluorophores.[1,41] NIR-II fluorescence images of the 143B osteosarcoma tumor-bearing mice were also captured after injecting **Yb-2** intravenously and no osteosarcoma fluorescence images were observed (Fig. S9†). This indicated that the complexes still need to be further modified for their application in tumor targeting. However, after 36 h tail vein injection, imaging of the femoral artery and major artery could still be performed (Fig. S10†), suggesting the long blood-circulation half-life of **Yb-2**. The high stability and long excretion time provide the possibility of utilizing the Yb^{3+} complexes for real-time visualization in long-time surgical operation, clinical diagnoses and biopsies.

Then we compared the NIR-II *in vivo* imaging resolution between **Yb-2** and **Yb-3** under the same conditions. Immediately after tail vein injection (150 μL, 3 mg ml^{-1}), NIR fluorescence images of the mice were captured. As shown in
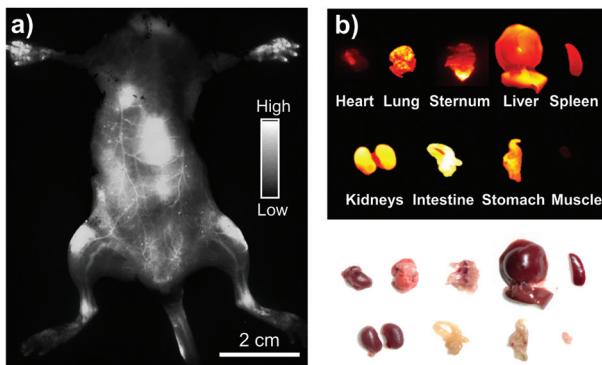
Fig. 4, the NIR-II image using **Yb-2** (Fig. 4a) displayed more small vessels compared to that obtained by **Yb-3** (Fig. 4b). The Gaussian-fit of the vessel FWHM (full width at half maxima) width is *ca.* 250.03 μm, with the signal-to-background ratio (SBR) of 2.49 ± 0.3 (Fig. 4c). However, compared to **Yb-2**, the NIR-II image of blood vessels using **Yb-3** showed a significant lower resolution (FWHM = 504.24 μm) and signal-to-background ratio (1.37 ± 0.1, Fig. 4d), likely due to the lower NIR quantum yield. This indicates the importance of NIR quantum yields in *in vivo* imaging resolution in the NIR-II region. Although the value of signal to background ratio is still slightly lower than that obtained using NIR-II luminescent organic molecules,[7,42] which should be due to the visible excitation wavelength, this can be improved by precise modulation of the porphyrin structures in the future.[24,43]

Considering the higher resolution and SBR of **Yb-2** than **Yb-3**, we chose **Yb-2** for further *in vivo* experiments. **Yb-2** was then injected in the footpads of nude mice at a prone position to explore its application in lymphoscintigraphy. One hour after the injection, high-bright contrast of the lymphatic vasculature and nodes was visualized clearly (Fig. 5). The popliteal lymph node-to-background ratios were observed to be 7.95 ± 0.3 and remained as high as 6.8 ± 0.2 even after 12 h injection. Moreover, the NIR-II measured lymph vessel had a Gaussian-fit diameter of *ca.* 591.7 μm and a SBR of *ca.* 2.59 ± 0.1 at 1 h, reflecting the transportation of the complexes through the lymphatic system. This revealed the potential application of the Yb^{3+} complexes in lymph related diagnoses and surgical operation.

NIR-II fluorophores have shown advantages in the real-time removal of sentinel lymph nodes and tumors at a higher spatial and temporal resolution, which is useful in "imaging-guided-operation".[1,2] Due to the high popliteal lymph node-to-tissue ratios of **Yb-2**, we then carried out the surgical resection of popliteal and sacral lymph nodes under the guidance of NIR-II imaging. As shown in Fig. 6, distinguished by the


Fig. 3 (a) Whole body NIR-II fluorescence images of **Yb-2** (150 μL, 3 mg ml^{-1}) after 5 min intravenous injection into C57BL/6 mice (λ_{ex}, 520 nm; λ_{em}, 1000 nm longpass filter; 3000 ms exposure; colour bar ranges from 5000 to 40 000, *n* = 3 per group); (b) *ex vivo* biodistribution studies at 12 h after the injection of **Yb-2**.
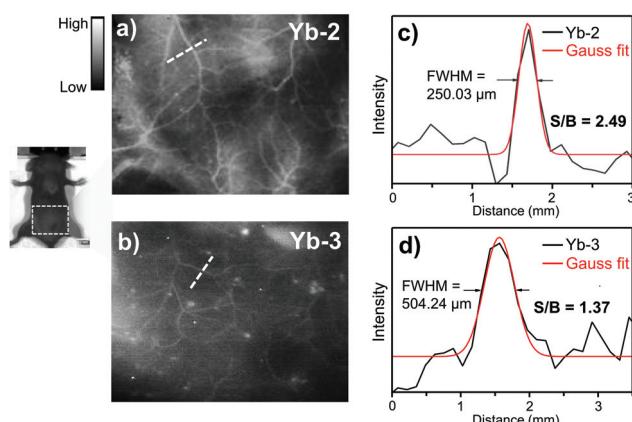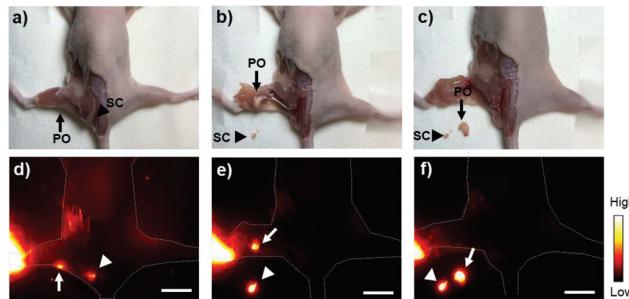
Fig. 4 Vasculature images of (a) **Yb-2** and (b) **Yb-3** (150 μL, 3 mg ml^{-1}) after 5 min intravenous injection into C57BL/6 mice (λ_{ex}, 520 nm; λ_{em}, 1000 nm longpass filter; 3000 ms exposure; colour bar ranges from 5000 to 40 000, *n* = 3 per group). Vessel FWHM width (white lines in (a) and (b)) and SBR analysis of (c) **Yb-2** and (d) **Yb-3**, based on the cross-sectional intensity profiles.

1964 | *Inorg. Chem. Front.*, 2019, **6**, 1962–1967

This journal is © the Partner Organisations 2019
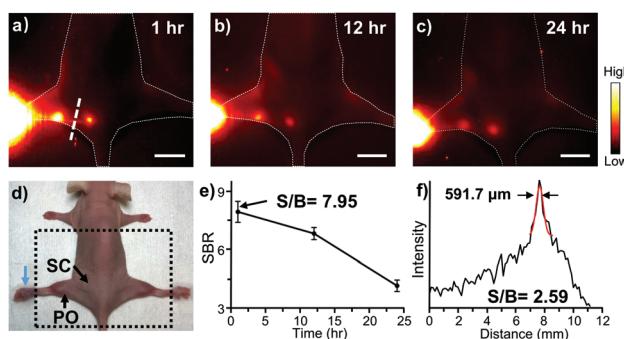
Fig. 5 (a), (b), (c) NIR-II fluorescence images ~1, 12, 24 hours post-injection of 3 mg ml^{-1} **Yb-2** in the left foot and PBS in the right foot (λ_{ex}, 520 nm; λ_{em}, 1000 nm longpass filter; 3000 ms exposure; color bar ranges from 100 to 25 000). (d) Photograph depicting a nude mouse at a prone position for imaging popliteal and sacral lymph nodes in (a), (b) and (c). Fluorophore injection sites indicated by blue arrows next to the footpad. (e) The popliteal lymph node-to-background ratios were determined with different timings after **Yb-2** injection. (f) The FWHM width and SBR (white lines in (a)) analysis of the lymph vessel based on the fluorescent cross-sectional intensity profiles. Scale bar: 1 cm.


Fig. 6 *In vivo* NIR-II image-guided popliteal and sacral lymph node mapping and biopsy. NIR-II fluorescence image at ~24 hour post-injection of 3 mg ml^{-1} **Yb-2** in the left foot of nude mice (*n* = 3 per group; λ_{ex}, 520 nm; λ_{em}, 1000 nm longpass filter; 1000 ms exposure; colour bar ranges from 1200 to 50 000). (a), (b), (c) Photograph depicting a nude mouse at a prone position for imaging popliteal (black arrow) and sacral (black arrowhead) lymph nodes by dissecting the skin in (a), then dissecting the muscles and exposing the lymph nodes in (b) and (c). (d), (e) and (f) The popliteal (white arrow) and sacral (white arrowhead) lymph nodes were clearly identified and dissected at their precise position in a short time. Scale bar: 1 cm.

higher fluorescence intensity, the popliteal and sacral lymph nodes can be easily and clearly identified and dissected at their prone position under the NIR-II imaging, successfully mimicking the standard SLNB procedure of clinical cancer surgery. Importantly, after the lymph nodes were resected, the operative field was clearly identified with NIR-II imaging, proving that no lymph nodes remained.

Conclusions

Taken together, we utilized highly luminescent water-soluble β-fluorinated Yb^{3+} complexes for *in vivo* NIR-II whole body bio-

imaging. Because of the deep penetration of the Yb^{3+} luminescence, the complex **Yb-2** was successfully applied in the non-invasive imaging of mice blood and lymphatic vasculatures and image-guided sentinel lymph node surgery in the NIR-II region, achieving a high signal-to-noise ratio. The metabolism mechanism of the Yb^{3+} complexes *in vivo* is similar to that of small organic molecules, excluding the slow excretion disadvantage of nanoparticles. As the luminescence of the lanthanide complex is metal-centered, it possesses higher photostability and environment irrelevant emission bands than traditional organic dyes. These results indicate that lanthanide complexes are highly promising and clinically translatable NIR-II fluorescence probes, paving a way to the design of metal coordination complexes for NIR-II fluorescence imaging and the study of NIR Ln^{3+} *in vivo* biology. Red-shifting the excitation wavelength to the NIR region and achieving tumor targeting are highly desirable in the next step, which are also currently under exploration in our lab.

Experimental section

General materials and methods

Unless otherwise stated, all reactions were performed under an inert atmosphere of nitrogen. UV-vis spectra were recorded on an Agilent 8453 UV-vis spectrometer equipped with an Agilent 89090A thermostat (±0.1 °C) at 25 °C. HeLa cells were obtained from the Peking University Health Science Center and incubated in complete medium (Dulbecco's modified Eagle's Medium, supplemented with 10% fetal bovine serum (FBS) and 1% penicillin–streptomycin) at 37 °C in an atmosphere containing 5% CO$_2$. Eight-week-old male C57BL/6 mice and nude mice were obtained from Charles River for animal studies and all animal procedures were performed under the approval of Stanford University's Administrative Panel on Laboratory Animal Care. For the optical measurements in liquid solution, spectroscopic-grade dimethyl sulfoxide was used as purchased from Alfa-Aesar. H$_2$O was obtained from Milli-Q integral. **Yb-1**, **Yb-2** and **Yb-3** were synthesized according to literature methods.[39,40]

Measurement of photophysical properties

Emission and excitation spectra and lifetimes were measured on an Edinburgh Analytical Instruments FLS980 lifetime and steady state spectrometer equipped with a 450 W Xe lamp, a 60 W microsecond flash lamp, PMT R928 for visible emission spectra, HAMAMATSU R5509-73 PMT with a C9940-02 cooler for NIR emission spectra and luminescence lifetime. Excitation and emission spectra were corrected for instrumental functions (including the correction for the detector, gratings *etc.*). Quantum yields were determined using a comparative method,[44] similar to previous studies.[39] The estimated error for the quantum yield measurements is 15%.

Cytotoxicity assay

HeLa cells were seeded in flat-bottomed 96-well plates, 10^4 cells per well, with 200 μL complete culture media in the dark for 24 h. Cells were incubated with 1–16 μM complexes for another 24 h in the dark while wells containing no cells were set as the controls. (For the measurement of photocytotoxicity: after washing three times with PBS, the cells were irradiated for 30 min in 100 μL PBS under the light irradiation (400–700 nm) with the same dose of light (6.5 mW cm^{-2}) for 30 min. Then PBS was replaced by 200 μL fresh culture media.) After culturing for 24 h, the cells were washed three times with PBS. Then 10 μL Cell Counting Kit-8 (CCK-8) solution and 90 μL PBS were added per well. After 30 min, the absorbance at 450 nm was read using a 96-well plate reader. The viability of HeLa cells was calculated by the following equation:

$$CV = (A_s - A_b)/(A_c - A_b) \times 100\% \qquad (1)$$

CV stands for the viability of cells, A_s, A_c and A_b stand for the absorbance of cells containing the studied complexes, cell control (no treated cells) and blank control (wells containing neither cells nor the studied complexes).

In vivo NIR-II fluorescence imaging

Mice were placed on a stage with a venous catheter for injection of contrast and imaging agents, and anesthesized using a 2 L min^{-1} oxygen flow with 2% isoflurane. The excitation laser was a 520 nm laser diode at a power density of 0.3 W cm^{-2} and emission was collected using a two-dimensional InGaAs array (Princeton Instruments) with a 1000 nm longpass filter. A lens set was used to obtain tunable magnifications ranging from 1× (whole body) to 2.5× (high magnification) magnification by changing the relative position of two NIR achromats (200 mm and 75 mm, Thorlabs). The exposure time for all images was 1000–3000 ms and images were processed with ImageJ.

Ex vivo biodistribution analysis

12 h after injection of **Yb-2**, nude mice were sacrificed and the major organs and tissues were collected. Then the NIR-II fluorescence images were obtained using a home-built NIR-II fluorescence imaging system with an InGaAs camera under illumination of a 520 nm laser diode at a power density of roughly 50 mW cm^{-2} and an exposure time of 500 ms.

Conflicts of interest

There are no conflicts to declare.

Acknowledgements

Notes and references

1 G. Hong, A. L. Antaris and H. Dai, *Nat. Biomed. Eng.*, 2017, **1**, 0010.

2 Q. Miao and K. Pu, *Adv. Mater.*, 2018, **30**, 1801778.

3 S. He, J. Song, J. Qu and Z. Cheng, *Chem. Soc. Rev.*, 2018, **47**, 4258–4278.

4 Y. Jiang and K. Pu, *Adv. Biosyst.*, 2018, **2**, 1700262.

5 A. L. Antaris, H. Chen, K. Cheng, Y. Sun, G. Hong, C. Qu, S. Diao, Z. Deng, X. Hu, B. Zhang, X. Zhang, O. K. Yaghi, Z. R. Alamparambil, X. Hong, Z. Cheng and H. Dai, *Nat. Mater.*, 2016, **15**, 235–242.

6 E. D. Cosco, J. R. Caram, O. T. Bruns, D. Franke, R. A. Day, E. P. Farr, M. G. Bawendi and E. M. Sletten, *Angew. Chem., Int. Ed.*, 2017, **56**, 13126–13129.

7 Q. Yang, Z. Hu, S. Zhu, R. Ma, H. Ma, Z. Ma, H. Wan, T. Zhu, Z. Jiang, W. Liu, L. Jiao, H. Sun, Y. Liang and H. Dai, *J. Am. Chem. Soc.*, 2018, **140**, 1715–1724.

8 Y. Jiang, P. K. Upputuri, C. Xie, Y. Lyu, L. Zhang, Q. Xiong, M. Pramanik and K. Pu, *Nano Lett.*, 2017, **17**, 4964–4969.

9 H. Gong, R. Peng and Z. Liu, *Adv. Drug Delivery Rev.*, 2013, **65**, 1951–1963.

10 C. Chen, P. Zhang, G. Gao, D. Gao, Y. Yang, H. Liu, Y. Wang, P. Gong and L. Cai, *Adv. Mater.*, 2014, **26**, 6313–6317.

11 M. Sakiyama, H. Sugimoto and M. Fujii, *Nanoscale*, 2018, **10**, 13902–13907.

12 Y. Lu, J. Lu, J. Zhao, J. Cusido, F. M. Raymo, J. Yuan, S. Yang, R. C. Leif, Y. Huo, J. A. Piper, J. Paul Robinson, E. M. Goldys and D. Jin, *Nat. Commun.*, 2014, **5**, 3741.

13 W. Zheng, D. Tu, P. Huang, S. Zhou, Z. Chen and X. Chen, *Chem. Commun.*, 2015, **51**, 4129–4143.

14 Y. Fan, P. Wang, Y. Lu, R. Wang, L. Zhou, X. Zheng, X. Li, J. A. Piper and F. Zhang, *Nat. Nanotechnol.*, 2018, **13**, 941–946.

15 I. Martinić, S. V. Eliseeva and S. Petoud, *J. Lumin.*, 2017, **189**, 19–43.

16 E. Thimsen, B. Sadtler and M. Y. Berezin, *Nanophotonics*, 2017, **6**, 1043–1054.

17 J.-C. G. Bünzli, *J. Lumin.*, 2016, **170**, 866–878.

18 C. G. Ma, M. G. Brik, D. X. Liu, B. Feng, Y. Tian and A. Suchocki, *J. Lumin.*, 2016, **170**, 369–374.

19 D. Parker, in *Handbook on the Physics and Chemistry of Rare Earths*, Elsevier, 2016, vol. 50, pp. 269–299.

20 M. Sy, A. Nonat, N. Hildebrandt and L. J. Charbonniere, *Chem. Commun.*, 2016, **52**, 5080–5095.

21 G. Mancino, A. J. Ferguson, A. Beeby, N. J. Long and T. S. Jones, *J. Am. Chem. Soc.*, 2005, **127**, 524–525.

22 C. Doffek, N. Alzakhem, C. Bischof, J. Wahsner, T. Guden-Silber, J. Lugger, C. Platas-Iglesias and M. Seitz, *J. Am. Chem. Soc.*, 2012, **134**, 16413–16423.

1966 | *Inorg. Chem. Front.*, 2019, **6**, 1962–1967

This journal is © the Partner Organisations 2019

23 W. Wu, X. Zhang, A. Y. Kornienko, G. A. Kumar, D. Yu, T. J. Emge, R. E. Riman and J. G. Brennan, *Inorg. Chem.*, 2018, **57**, 1912–1918.

24 S. Luo, E. Zhang, Y. Su, T. Cheng and C. Shi, *Biomaterials*, 2011, **32**, 7127–7138.

25 A. D'Aleo, A. Bourdolle, S. Brustlein, T. Fauquier, A. Grichine, A. Duperray, P. L. Baldeck, C. Andraud, S. Brasselet and O. Maury, *Angew. Chem., Int. Ed.*, 2012, **51**, 6622–6625.

26 A. Foucault-Collet, K. A. Gogick, K. A. White, S. Villette, A. Pallier, G. Collet, C. Kieda, T. Li, S. J. Geib, N. L. Rosi and S. Petoud, *Proc. Natl. Acad. Sci. U. S. A.*, 2013, **110**, 17199–17204.

27 A. Foucault-Collet, C. M. Shade, I. Nazarenko, S. Petoud and S. V. Eliseeva, *Angew. Chem., Int. Ed.*, 2014, **53**, 2927–2930.

28 I. Martinic, S. V. Eliseeva, T. N. Nguyen, V. L. Pecoraro and S. Petoud, *J. Am. Chem. Soc.*, 2017, **139**, 8388–8391.

29 M. A. Alcala, C. M. Shade, H. Uh, S. Y. Kwan, M. Bischof, Z. P. Thompson, K. A. Gogick, A. R. Meier, T. G. Strein, D. L. Bartlett, R. A. Modzelewski, Y. J. Lee, S. Petoud and C. K. Brown, *Biomaterials*, 2011, **32**, 9343–9352.

30 E. M. Surender, S. Comby, B. L. Cavanagh, O. Brennan, T. C. Lee and T. Gunnlaugsson, *Chem*, 2016, **1**, 438–455.

31 W. Yang, L. M. Fu, X. Wen, Y. Liu, Y. Tian, Y. C. Liu, R. C. Han, Z. Y. Gao, T. E. Wang, Y. L. Sha, Y. Q. Jiang, Y. Wang and J. P. Zhang, *Biomaterials*, 2016, **100**, 152–161.

32 H. Ma, B. Song, Y. Wang, D. Cong, Y. Jiang and J. Yuan, *Chem. Sci.*, 2017, **8**, 150–159.

33 A. T. Frawley, H. V. Linford, M. Starck, R. Pal and D. Parker, *Chem. Sci.*, 2018, **9**, 1042–1049.

34 S. Comby and J. C. G. Bünzli, *Lanthanide near-infrared luminescence in molecular probes and devices*, Elsevier, Amsterdam, 2007.

35 V. Pansare, S. Hejazi, W. Faenza and R. K. Prud'homme, *Chem. Mater.*, 2012, **24**, 812–827.

36 S. J. Bradberry, A. J. Savyasachi, M. Martinez-Calvo and T. Gunnlaugsson, *Coord. Chem. Rev.*, 2014, **273–274**, 226–241.

37 J. Y. Hu, Y. Ning, Y. S. Meng, J. Zhang, Z. Y. Wu, S. Gao and J. L. Zhang, *Chem. Sci.*, 2017, **8**, 2702–2709.

38 J. Y. Hu, Z. Y. Wu, K. Chai, Z. S. Yang, Y. S. Meng, J. Zhang and J. L. Zhang, *Inorg. Chem. Front.*, 2017, **4**, 1539–1545.

39 Y. Ning, J. Tang, Y. W. Liu, J. Jing, Y. Sun and J. L. Zhang, *Chem. Sci.*, 2018, **9**, 3742–3753.

40 Y. Ning, S. Cheng, J.-X. Wang, Y.-W. Liu, W. Feng, F. Li and J.-L. Zhang, *Chem. Sci.*, 2019, **10**, 4227–4235.

41 F. Ding, Y. Zhan, X. Lu and Y. Sun, *Chem. Sci.*, 2018, **9**, 4370–4380.

42 Z. M. Tao, G. S. Hong, C. Shinji, C. X. Chen, S. Diao, A. L. Antaris, B. Zhang, Y. P. Zou and H. J. Dai, *Angew. Chem., Int. Ed.*, 2013, **52**, 13002–13006.

43 R. Xiong, D. Mara, J. Liu, R. Van Deun and K. E. Borbas, *J. Am. Chem. Soc.*, 2018, **140**, 10975–10979.

44 H. J. Yvon, A Guide to Recording Fluorescence Quantum Yields, HORIBA Jobin Yvon Inc, Stanmore, Middlesex, UK, 2012.